

THE SWIMMING OF UNIPOLAR CELLS OF *SPIRILLUM VOLUTANS*: THEORY AND OBSERVATIONS

M. RAMIA^{1,*} AND M. A. SWAN²

¹*Department of Mechanical Engineering and* ²*Department of Anatomy and Histology,*
University of Sydney, NSW 2006, Australia

Accepted 25 August 1993

Summary

Bright-field high-speed cinemicrography was employed to record the swimming of six unipolar cells of *Spirillum volutans*. A complete set of geometrical parameters for each of these six cells, which are of typical but varying dimensions, was measured experimentally. For each cell, the mean swimming linear and angular speeds were measured for a period representing an exact number of flagellar cycles (at least four and up to 12 cycles). Two independent sets of measurements were carried out for each cell, one relating to the trailing and the other to the leading configuration of the flagellar bundle. The geometry of these cells was numerically modelled with curved isoparametric boundary elements (from the measured geometrical parameters), and an existing boundary element method (BEM) program was applied to predict the mean swimming linear and angular speeds. A direct comparison between the experimentally observed swimming speeds and those of the BEM predictions is made. For a typical cell, a direct comparison of the swimming trajectory, in each of the trailing and the leading flagellar configurations, was also included. Previous resistive force theory (RFT) as well as slender body theory (SBT) models are both restricted to somewhat non-realistic 'slender body' geometries, and they both fail to consider swimming kinematics. The present BEM model, however, is applicable to organisms with arbitrary geometry and correctly accounts for swimming kinematics; hence, it agrees better with experimental observations than do the previous models.

Introduction

It is generally accepted that bacteria propel themselves through fluids by rotating a flagellum or a flagellar bundle (several flagellar filaments which rotate together as a single unit) (Berg and Anderson, 1973). Meister *et al.* (1989) recently studied the molecular rotary motor which rotates each filament, at its base, relative to the cell body. Previous observations of bacterial propulsion by cinemicrography used dark-field illumination (see Mussill and Jarosch, 1972; Shimada *et al.* 1976; Winet and Keller, 1976, for example).

*Present address: School of Mechanical and Manufacturing Engineering, The University of New South Wales, Kensington, NSW 2033, Australia.

Key words: swimming kinematics, cinemicrography, boundary element, bacterial flagella, *Spirillum volutans*.

With dark-field microscopy, light scattered by the cell body obscures the flagellum as it rotates about the cell body. Furthermore, such observations used slow filming rates and therefore had difficulty in accurately resolving the cell body and flagellar rotation. In the present study, fast filming rates ($350\text{--}530\text{ frames s}^{-1}$) and phase-contrast bright-field cinemicrography were used to overcome these difficulties.

Spirillum volutans is a gram-negative bacterium with a group of flagellar filaments, termed a flagellar bundle, emanating from either or both ends of its rigid helical cell body. Each flagellar filament inserts into a flagellar base in the cytoplasm. The ultrastructure of the flagellar bases is quite complex (Swan, 1985). Typically, an old cell of *S. volutans* possesses a flagellar bundle at each end of its long (in excess of 2 wavelengths) cell body and hence is said to be bipolar. Multiplication of this organism takes place when an old bipolar cell divides to form two shorter unipolar cells.

Depending on the sense of the flagellar rotation, a unipolar cell may assume a leading flagellar position (with the flagellum drawing the cell body behind it) or a trailing position (with the flagellum impelling the cell body in front of it). These are referred to as leading and trailing configurations, respectively. The present study considers the experimental observation and numerical modelling of unipolar *S. volutans* swimming in both the leading and the trailing configurations.

From a simplified modelling point of view, this micro-organism may be considered to consist of an inert cell body and a helical flagellar bundle (hereafter referred to as a flagellum for convenience), which rotates relative to the cell body with a presumed constant angular velocity ω . As a result of this rotation, the flagellum induces a net force and a net moment on the cell body. Hence, the entire organism acquires an instantaneous rigid-body swimming velocity \mathbf{U} and counter-rotation angular velocity $\mathbf{\Omega}$ to maintain equilibrium. The locomotion problem is concerned with the prediction of \mathbf{U} , $\mathbf{\Omega}$ and the mean swimming speed \bar{U} for a given geometry of the organism, flagellar wave parameters and viscosity of the surrounding fluid.

Chwang *et al.* (1972) modelled the swimming of this organism by replacing the effect of the surrounding fluid with a pair of coefficients representing the respective hydrodynamic resistances to motions normal and tangential to the cell body and flagellar centrelines. This method is known as the resistive force theory (RFT) approach and was first formulated by Gray and Hancock (1955). Although it was later refined by Lighthill (1976), it is limited to micro-organisms that can be modelled by a combination of slender bodies (i.e. bodies possessing small curvature and cross-sectional dimensions compared with their lengths) and spheroids. Furthermore, it fails to account for hydrodynamic interaction between the cell body and the flagellum. Cinemicrographs of *Spirilla* (Swan, 1982) suggest that their cell bodies are neither slender nor spheroidal; hence the need for an alternative approach.

Myerscough and Swan (1989) considered a distribution of singularities (Stokeslets and doublets) along the centrelines of the cell body and flagellum, both modelled as cylindrical filaments. By satisfying the no-slip conditions at the boundary (i.e. the organism's surface), together with the equilibrium conditions, the strengths of the singularities and the velocities \mathbf{U} and $\mathbf{\Omega}$ can be solved for simultaneously. This method, known as the slender body theory (SBT) approach, was first formulated by Hancock

(1953), and has since been refined by many other workers in the field, such as Cox (1970), Higdon (1979a) and Johnson (1980). Unlike Chwang *et al.* (1972), Myerscough and Swan (1989) allowed for finite transverse components of \mathbf{U} and $\mathbf{\Omega}$, which are of major significance in modelling the locomotion of *Spirilla*. Hydrodynamic interaction is also accounted for by including the relevant image systems for the respective singularities.

Both of the above-mentioned models assume the flagellum to be a straight, rigid rod rotating at an angle to the cell body axis, hence defining a conical surface of revolution. Furthermore, the slender body assumption restricts both models to somewhat unrealistic proportions for the organism.

Ramia (1991) modelled the swimming of *S. volutans* using the boundary element method (BEM) as documented by Youngren and Acrivos (1975). Being applicable to arbitrary geometries, the BEM allowed an extensive optimisation study involving variations in a full range of geometrical parameters. This was coupled with a comprehensive kinematic scheme – basically, a numerical generalisation of the method of Keller and Rubinow (1976) – to predict the swimming trajectory and consequently the mean swimming speed \bar{U} . The resulting organism, with the deduced optimum dimensions, closely resembled the efficiently swimming real organism as experimentally observed (see, for example, Swan, 1982). However, a more direct comparison with experimental observations was not made.

The present study is concerned with the experimental observation of six unipolar *S. volutans* cells and the direct comparison of the measured swimming speeds with the corresponding BEM numerical predictions for each cell. We utilised the above-mentioned BEM model of Ramia (1991) and discretised the organism's surface into curved parabolic boundary elements rather than flat constant elements. The relevant numerical procedure is discussed at greater length by Ramia *et al.* (1993) and Brebbia *et al.* (1984), and only a brief description is given here.

Numerical model

The Reynolds number associated with the swimming of micro-organisms is typically of the order 10^{-2} or less. This allows inertial forces to be neglected (reviewed by Brennen and Winet, 1977). Furthermore, body forces can also be neglected and the conservation equations can be reduced to those of Stokes flow. A boundary element formulation is used to solve these equations, for the boundary tractions (i.e. the force acting on a given element divided by the surface area of that element), with the appropriate boundary conditions, namely the no-slip condition on the surface of the organism and the vanishing fluid disturbance at infinity. The governing equations may be expressed in the form:

$$\eta \nabla^2 \mathbf{u} = \nabla p, \quad \nabla \mathbf{u} = 0, \quad (\mathbf{x} \in \mathbf{V}) \quad (1)$$

where \mathbf{u} is the velocity vector, p is the hydrostatic pressure, η is the viscosity of the fluid and \mathbf{V} is the flow domain.

For a body discretised into N collocation points (nodes), Brebbia *et al.* (1984) relate the boundary tractions \mathbf{t} to the velocity boundary conditions \mathbf{u} using the expression:

$$\mathbf{H}\mathbf{u} = \mathbf{G}\mathbf{t}, \quad (2)$$

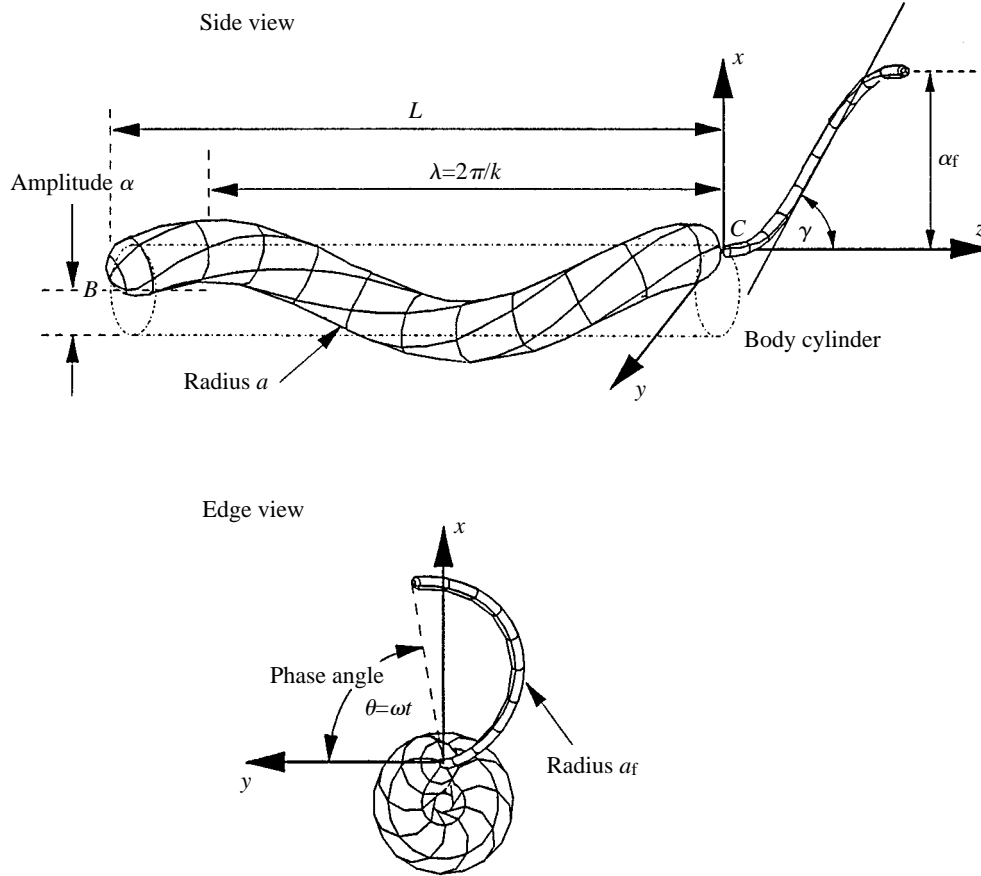


Fig. 1. Definition of the geometrical parameters used to model the *Spirillum volutans* cell.

where \mathbf{H} and \mathbf{G} are known $3N \times 3N$ matrices depending only on the geometry of the boundary. Here, the velocity and traction vectors (each of dimension $3N$) are arranged such that u_1, u_2, u_3 are the velocity components at node 1; t_1, t_2, t_3 are the traction components at node 1; u_4, u_5, u_6 are the velocity components at node 2, etc. Furthermore, the traction over a given element is given in terms of the nodal tractions *via* a quadratic interpolation function. Presently, only two types of boundary elements are employed; triangular elements with six nodes or rectangular elements with eight nodes (Bathe, 1982), both being curved isoparametric quadratic elements.

Geometrical modelling

Fig. 1 shows a geometric representation of a unipolar *S. volutans* with a trailing flagellar configuration. This organism has a cell body of cross-sectional radius a and length l , which is curved to form a helix of axial length L , wavelength λ and amplitude α . The trailing flagellum has an amplitude α_f , cross-sectional radius a_f and length l_f . This flagellum rotates to form a flagellar cone angle γ , as depicted in Fig. 2.

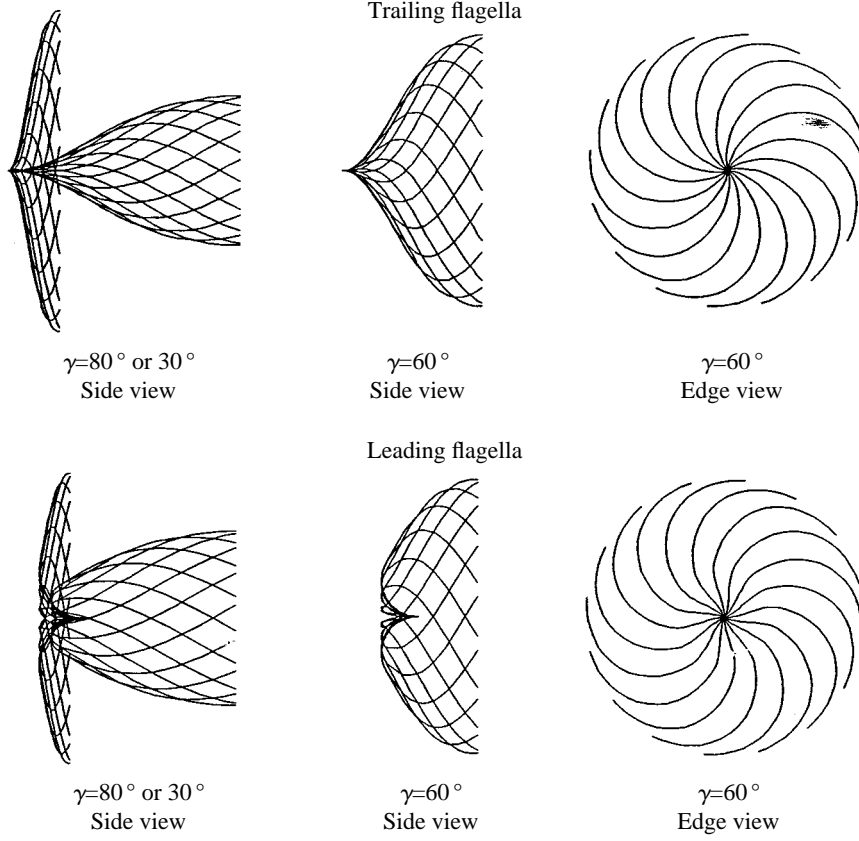


Fig. 2. Position of flagellar centrelines at 16 distinct phase angles θ for various cone angles γ .

The centreline of the cell body is defined by the position vector \mathbf{r} . When referred to the (x, y, z) axes, whose z -axis is parallel to the cell body axis and consequently to the flagellar axis of rotation, this is given by Ramia (1991) as:

$$\mathbf{r} = \left\{ 2\alpha \cos \left[k \left(\frac{z+2L}{2} \right) \right] \sin \left(\frac{kz}{2} \right), \right. \\ \left. 2\alpha \sin \left[k \left(\frac{z+2L}{2} \right) \right] \sin \left(\frac{-kz}{2} \right), z \right\}, \quad -L \leq z \leq 0. \quad (3)$$

The position vector \mathbf{r}_f defining the flagellar centreline may, referred to the (x, y, z) axes, be expressed in the form:

$$\mathbf{r}_f = [\alpha_f E(z) \cos(k_f z + \theta), \\ \alpha_f E(z) \sin(k_f z + \theta), z], \quad 0 \leq z \leq z_e, \quad (4)$$

where α_f , θ , k_f and z_e are the amplitude, phase angle, wavenumber and axial length of the (right-handed) flagellar helix, respectively. $E(z)$ is an amplitude-modifying function (as

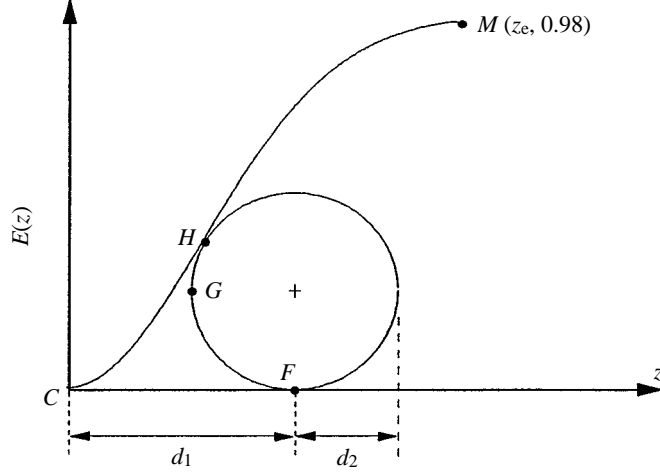


Fig. 3. Functions defining the leading and trailing flagellar amplitude envelopes.

shown in Fig. 3), which is described by the line *CHM* for the trailing flagellar case and the line *FGHM* for the leading flagellar case.

For the line *CHM*, the amplitude function:

$$E(z) = 1 - \exp[-(k_e z)^2], \quad (5)$$

of Higdon (1979b) has been adopted, where k_e is a constant determining the rate at which $E(z)$ grows asymptotically to its maximum value of 1. It is found that an appropriate choice for k_e and z_e gives rise to an amplitude envelope which realistically models the trailing flagellar geometry. Allowing the amplitude function to grow to 0.98 and equating γ to the slope $E'(z)$ at the point of inflection $H[(k_e \sqrt{2})^{-1}, 1 - e^{-1/2}]$ gives rise to the respective constraints:

$$\begin{aligned} z_e &= \frac{2}{k_e}, \\ k_e \sqrt{2} e^{-1/2} &= \tan \gamma, \end{aligned} \quad (6)$$

which, for a given value of γ , uniquely specify k_e and z_e .

The helical wave parameters α_f and k_f should be specified subject to the condition of a constant number of flagellar wavelengths for all given flagellar cone angles γ . It is found that assuming $\alpha_f k_f = \tan \gamma$ (which allows for approximately 0.27 wavelengths) yields the most acceptable qualitative agreement between trailing flagellar geometries as given by equation 4, depicted in Fig. 2, and the present experimental observations (see also, for example, Fig. 5 of Winet and Keller, 1976). Because a value of 1 for α_f is taken to be the fundamental common dimension for all organism discretisations, γ is the only remaining wave parameter for the trailing flagellum *CHM*.

For the leading flagellar case, the portion CH is replaced by a circular arc FGH of radius d_2 and centre (d_1, d_2) . Here, equation 5 is replaced by:

$$E(z) = d_2 + \delta \sqrt{d_2^2 - (z - d_1)^2}, \quad \begin{cases} \delta = -1 & \text{for points on } FG, \\ \delta = 1 & \text{for points on } GH. \end{cases} \quad (7)$$

Imposing continuity of $E(z)$ and $E'(z)$ at H gives the parameters d_1 and d_2 as:

$$\begin{aligned} d_1 &= \frac{1}{k_e \sqrt{2}} + d_2 \sqrt{\frac{2k_e^2}{e + 2k_e^2}}, \\ d_2 &= \left(\frac{e + 2k_e^2}{2k_e^2} \right) (1 - e^{-1/2}) \left(1 - \sqrt{1 - \frac{2k_e^2}{e + 2k_e^2}} \right). \end{aligned} \quad (8)$$

The flagellar length l_f is given in general form by the integral:

$$l_f = \int_{z_1}^{z_u} \sqrt{1 + [\alpha_f k_f E(z)]^2 + [\alpha_f E'(z)]^2} dz, \quad (9)$$

which, given suitable choices for $E(z)$ and the limits z_1 and z_u , can be solved numerically to obtain the trailing or leading flagellar lengths. The resulting flagellar centreline geometry, for both leading and trailing configurations with various cone angles at 16 different phase angles, is depicted in Fig. 2.

The geometry at a given instant is fully specified by the nine parameters α , k , N_λ , γ , l_f , l , a_f , a and the flagellar phase angle θ relative to the cell body, as defined in Fig. 1. Based on the similar model of Ramia (1991), these are expressed as seven dimensionless parameters: αk , N_λ , γ , l_f/l , a/l , a_f/a and θ .

The flagellar amplitude α_f is assigned a value of 1 throughout and the flagellar cone angle γ is specified, which, from equations 6, gives k_e and z_e . Equations 5 and 7 then define the flagellar amplitude functions $E(z)$, and the flagellar length l_f is calculated from equation 9. Next, l_f/l is specified, giving the cell body length l , and then the parameters k , N_λ and θ are specified. The axial extension L is calculated as $l/\sqrt{1 + (\alpha k)^2}$ and equations 3 and 4 then define the cell body and flagellar centrelines. Finally, the cell body and flagellar radii are specified using the parameters a/l and a_f/a .

The equations defining the cell body and flagellar surfaces may then be given as functions of their respective centreline geometries and of radii a and a_f (see Phan-Thien *et al.* 1987). The cell body and flagellar surfaces are then discretised into curved parabolic isoparametric elements as outlined briefly in Appendix 1 and discussed in greater detail by Ramia *et al.* (1993).

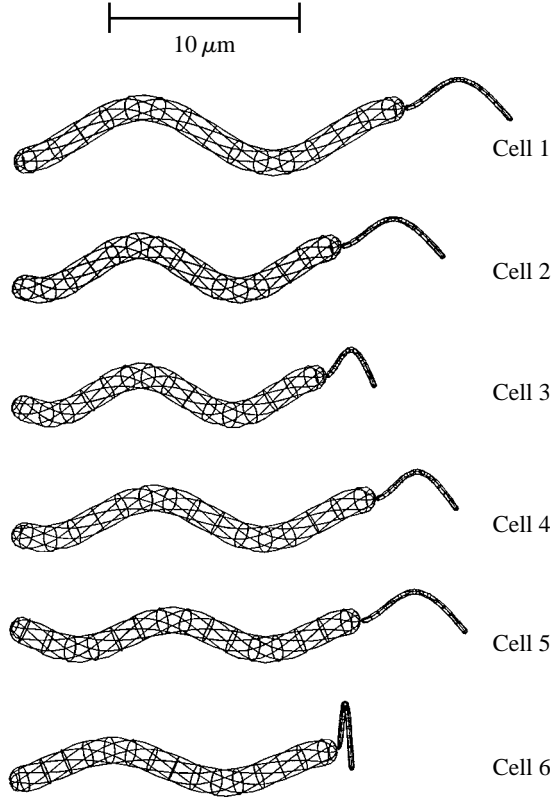
The measured geometrical parameters for each of the six cells are summarised in Table 1, and the discretised representations of these organisms in relation to a $10 \mu\text{m}$ scale bar are shown in Fig. 4. For each of these, a flagellar phase angle of zero is assumed.

Instantaneous velocities

The flagellum and the cell body of the organism are considered as separate individual bodies (i.e. closed surfaces). The flagellum is given a rotation with an angular velocity,

Table 1. *Summary of the measured and calculated geometrical parameters for each of the six cells*

Parameter	Cell 1	Cell 2	Cell 3	Cell 4	Cell 5	Cell 6
$k (\mu\text{m}^{-1})$	0.4520	0.5872	0.6347	0.5370	0.6283	0.5325
αk	0.6780	0.7046	0.6982	0.5907	0.4901	0.4473
N_λ	1.4892	1.6262	1.6970	1.6410	1.8600	1.4576
$l_f (\mu\text{m})$	8.2891	7.8899	6.0649	6.9692	8.1812	9.2921
$l (\mu\text{m})$	25.009	21.285	20.490	22.300	20.714	18.842
l_f/l	0.3314	0.3707	0.2960	0.3125	0.3950	0.4932
γ (trailing) (degrees)	49	48	66	54	49	86
γ (leading) (degrees)	66	68	86	80	62	66
a/l	0.0283	0.0333	0.0346	0.0318	0.0342	0.0376
a_f/a	0.2	0.2	0.2	0.2	0.2	0.2

Fig. 4. Boundary element discretisations of the six cells as modelled in the trailing flagellar configuration. All cell dimensions are to scale, have a flagellar phase angle of zero and are viewed in the X - Z plane.

having a constant magnitude ω , about the flagellar axis relative to the cell body. By integrating the boundary tractions over the appropriate surfaces, a resistance matrix defining the force per unit velocity of the two-body system is compiled. The relevant kinematic and

equilibrium constraints are then used to solve for the instantaneous velocities. These velocities are determined as functions of time for a complete flagellar cycle.

The viscous force \mathbf{F} and torque \mathbf{T} acting on a body (or particle) k defined by the closed surface S_k are given by the integrals:

$$\mathbf{F} = \oint_{S_k} \mathbf{t} dS$$

and

$$\mathbf{T} = \oint_{S_k} (\mathbf{x} \times \mathbf{t}) dS, \quad (10)$$

where \mathbf{x} represents the displacement vector from the cell body/flagellar joining point C .

Using equations 2 and 10, a series of 12 numerical experiments may be carried out enabling the calculation of the elements comprising the resistance matrix in the following equation (Happel and Brenner, 1973):

$$\begin{pmatrix} \mathbf{F}_1 \\ \mathbf{T}_1 \\ \mathbf{F}_2 \\ \mathbf{T}_2 \end{pmatrix} = \begin{pmatrix} \mathbf{K}_{11} & \mathbf{A}_{11} & \mathbf{K}_{12} & \mathbf{A}_{12} \\ \mathbf{L}_{11} & \mathbf{M}_{11} & \mathbf{L}_{12} & \mathbf{M}_{12} \\ \mathbf{K}_{21} & \mathbf{A}_{21} & \mathbf{K}_{22} & \mathbf{A}_{22} \\ \mathbf{L}_{21} & \mathbf{M}_{21} & \mathbf{L}_{22} & \mathbf{M}_{22} \end{pmatrix} \begin{pmatrix} \mathbf{U}_1 \\ \boldsymbol{\Omega}_1 \\ \mathbf{U}_2 \\ \boldsymbol{\Omega}_2 \end{pmatrix}, \quad (11)$$

where the cell body and flagellum are referred to by the subscripts 1 and 2 respectively. Each element in the above matrix is itself a 3×3 matrix because each of the forces, torques, velocities and angular velocities is a three-dimensional vector. Typically for example, A_{ijkl} is the force in the i direction on the particle k due to the angular rotation (with a unit angular velocity) of particle l in the j direction. Similar definitions follow for K_{ijkl} , L_{ijkl} and M_{ijkl} . The indices i and j are cycled through the usual x, y, z directions, whereas k and l can each be assigned either of the values 1 or 2 (i.e. cell body or flagellum).

The flagellum rotates relative to the cell body with an angular velocity $\boldsymbol{\omega} = (0, 0, \omega)$ ($|\omega|$ is assigned a value of 1 and is used as a normalising factor), whilst the whole organism translates rigidly with velocity \mathbf{U} . This gives rise to the kinematic constraints:

$$\mathbf{U}_1 = \mathbf{U}_2$$

and

$$\boldsymbol{\Omega}_1 = \boldsymbol{\Omega}_2 - \boldsymbol{\omega} \quad (12)$$

The equilibrium requirement:

$$\mathbf{F}_1 = -\mathbf{F}_2$$

and

$$\mathbf{T}_1 = -\mathbf{T}_2 \quad (13)$$

furnishes the remaining two of the eight necessary vector equations (equations 11–13) for which the eight vectors \mathbf{F}_1 , \mathbf{T}_1 , \mathbf{F}_2 , \mathbf{T}_2 , \mathbf{U}_1 , $\boldsymbol{\Omega}_1$, \mathbf{U}_2 and $\boldsymbol{\Omega}_2$ may be solved. Of particular interest are the instantaneous linear velocity $\mathbf{U} = \mathbf{U}_1$ and instantaneous angular velocity $\boldsymbol{\Omega} = \boldsymbol{\Omega}_1$ of the cell body or, in more general terms, of the organism.

This procedure may easily be generalised to model an n -organism system by simply

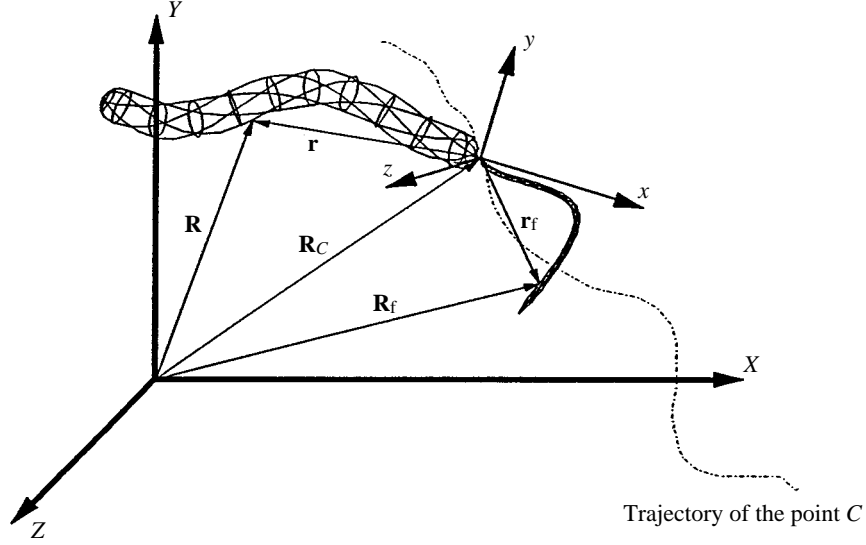


Fig. 5. Definition of the variables and axes associated with the modelling of swimming kinematics.

increasing the range of the indices k and l up to $2n$ and applying the kinematic and equilibrium constraints to each cell body/flagellar pair of particles. An application of this may be found in Ramia *et al.* (1993), who used this general procedure to study the hydrodynamic interaction between two organisms swimming close and parallel to each other.

Swimming kinematics

Let $\mathbf{r}(t)$ represent any position vector in the cell-body-fixed (x, y, z) frame (i.e. a frame at rest with respect to the cell body which will hereafter be referred to as the body frame) and $\mathbf{R}(t)$ be this vector referred to the globally fixed (X, Y, Z) frame (see Fig. 5) at a given time t . The transformation from $\mathbf{r}(t)$ to $\mathbf{R}(t)$ consists of a translation by $\mathbf{R}_C(t)$ and a rotation by $\mathbf{A}^{-1}(t)$ (Keller and Rubinow, 1976):

$$\begin{aligned} \mathbf{R}(t) &= \mathbf{R}_C(t) + \mathbf{A}^{-1}(t)\mathbf{r}(t), \\ \frac{d\mathbf{R}_C(t)}{dt} &= \mathbf{A}^{-1}(t)\mathbf{U}(t). \end{aligned} \quad (14)$$

The matrix \mathbf{A}^{-1} is a 3×3 rotation matrix expressible in terms of the Euler angles $\psi_1(t)$, $\psi_2(t)$ and $\psi_3(t)$ (equation 4-47 in Goldstein, 1950). These angles in turn depend on the angular velocity of the body frame $\boldsymbol{\Omega}$ according to the differential equations (equations 4-103 in Goldstein, 1950):

$$\boldsymbol{\Omega} = \{ \dot{\psi}_1 \sin \psi_3 \sin \psi_2 + \dot{\psi}_2 \cos \psi_3, \quad \dot{\psi}_1 \sin \psi_2 \cos \psi_3 - \dot{\psi}_2 \sin \psi_3, \quad \dot{\psi}_1 \cos \psi_2 + \dot{\psi}_3 \}, \quad (15)$$

where the dot notation is used to represent time derivatives. Numerical solution of these equations (with appropriate initial conditions) for the Euler angles specifies the rotation

matrix \mathbf{A}^{-1} giving the trajectory of the cell body/flagellar joining point (i.e. the origin) and any point in the body frame \mathbf{R}_f from equations 14. Points on the flagellum rotate with an angular velocity $\boldsymbol{\omega}$ relative to the body frame and may easily be referred to it. The coordinates of such points can, in turn, be referred to the fixed frame using the first of equations 14 giving the trajectory of any point on the flagellar surface.

Mean swimming speeds

The flowchart of Fig. 6 gives an outline of the steps involved in determining the mean swimming speed \bar{U} . Initially, the organism's flagellar phase angle θ as well as its position and orientation relative to the globally fixed (X,Y,Z) frame are specified. Using the BEM, the instantaneous velocities \mathbf{U} and $\boldsymbol{\Omega}$ are then calculated. Next, the flagellar phase angle is incremented (in the same sense as the fundamental flagellar rotation), giving a new flagellar orientation, relative to the supposedly fixed cell body, and again the BEM is used to re-solve the Stokes problem for the updated geometry and boundary conditions. In this manner, the entire flagellar cycle is scanned and \mathbf{U} and $\boldsymbol{\Omega}$ may then be expressed as discrete functions of θ (where $\theta = \omega t$ and $\omega = 1$ throughout). A least-squares regression transforms these into continuous functions of θ . Reference of these functions to the globally fixed (X,Y,Z) frame and substitution into equations 14–15 yields the trajectory of any point on the organism. The direction cosines of the flagellar axis are averaged over the time interval considered (here 16π , which represents eight flagellar cycles). These averages represent the direction cosines of the axis of propagation. An axial velocity is defined as the ratio of the displacement along the axis of propagation to the elapsed time. It is found that, in all the cases considered, this velocity varies periodically with every flagellar cycle. Over the specified time interval, which is significantly larger than, and an exact multiple of, the flagellar period 2π , the mean of this axial velocity defines the mean swimming speed \bar{U} .

The mean angular velocity is simply defined as $\bar{\Omega} = (\bar{U}_x^2 + \bar{U}_y^2 + \bar{U}_z^2)^{1/2}$ with \bar{U}_x , \bar{U}_y and \bar{U}_z representing the means of the respective components for one flagellar cycle. This definition is sufficient as \bar{U}_x and \bar{U}_y are both small compared with \bar{U}_z .

Experimental procedure

Spirillum volutans, American Type Culture Collection (ATCC) catalogue no. 19554, was grown at 30 °C in ATCC medium 234. An actively growing culture was used in order to obtain a high proportion of unipolar cells. The preparation was placed on a slide with a number 1.5 coverslip supported by petroleum jelly to provide a good depth of fluid and to avoid fluid drift. A fan heater was used to warm this preparation to 28 °C. The light source was a wild Xenon arc 150 W XBO lamp (Leica Instruments, North Ryde, NSW) with additional ultraviolet filters to protect the cells. The film exposure was adjusted *via* neutral density filters. Observations were recorded on 16 mm Ilford Pan F type 752 negative film, using a Locam camera (Redlake Corp., Campbell, CA) and a Carl Zeiss WL microscope with a rotating and gliding stage. Objectives used were 40/0.75 neofluar or 63/1.4 planapochromat. The framing rates ranged from 350 to 530 frames s⁻¹, with 500 frames s⁻¹ being used in most cases. The interval between the frames was recorded

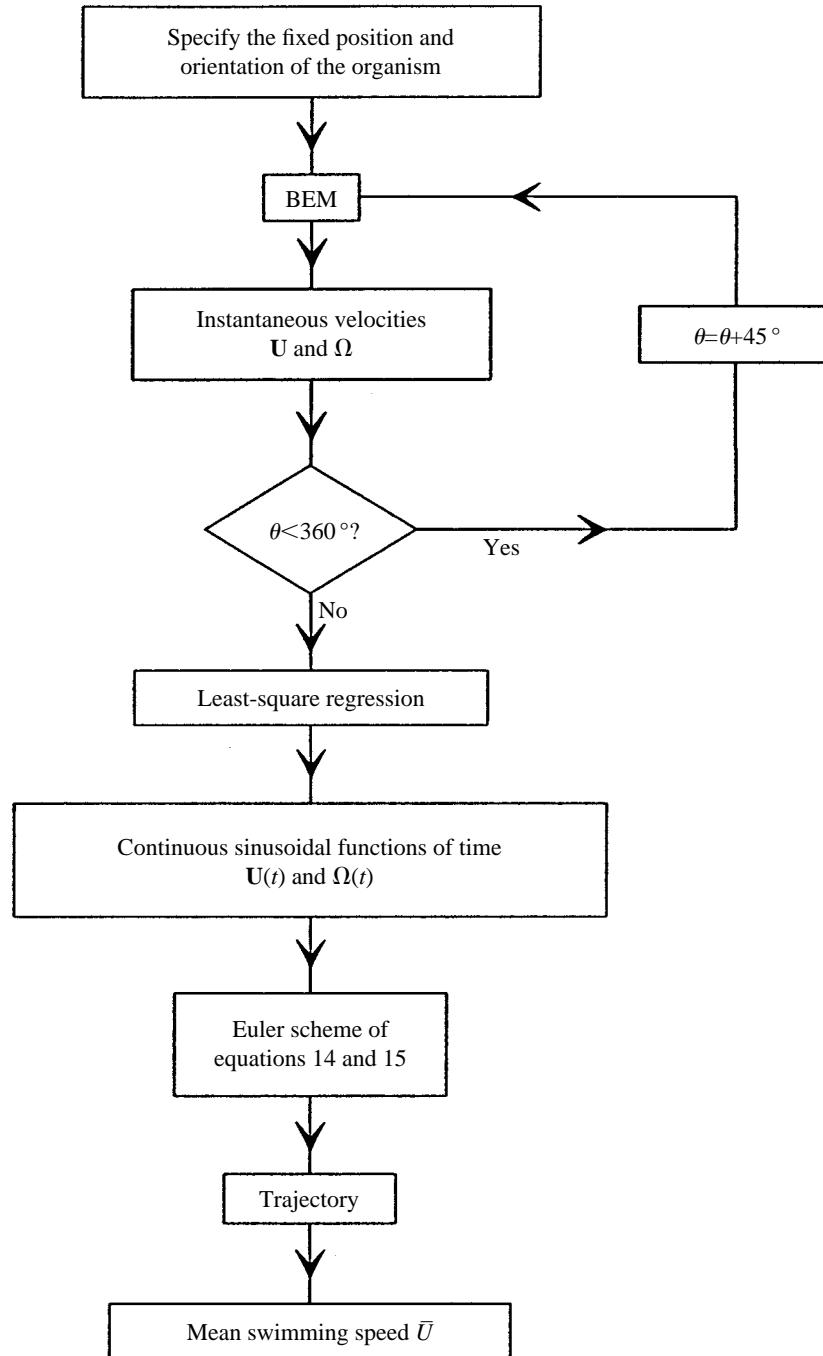


Fig. 6. Flowchart outlining the steps involved in predicting the swimming trajectory and mean swimming speed.

with a timing light within the camera. The films were analyzed using 16 mm positive cineprints magnified with a projector (L.W. International, Woodland Hills, CA) *via* front-surfaced mirrors onto a drawing area. Consecutive frames were aligned with an ocular graticule.

Measurements were made for each bacterium throughout at least four and up to 12 consecutive cycles of flagellar rotation. Only sequences with a given unipolar cell swimming isolated from neighbouring cells were considered. Furthermore, measurements were carried out only on cells with both poles of the cell body in focus at some time during the sequence to ascertain that they were unipolar. Two sets of measurements were taken for the trailing and for the leading configurations. During reorientation from the trailing to the leading configuration, or *vice versa*, the flagellar bundle did not fly apart, which is in contrast to tumbling bacteria (Macnab and Ornston, 1977).

The flagellar amplitude α_f and cone angle γ were measured by superimposing tracings of the flagellar bundle centreline from consecutive frames. Each tracing was aligned with the previous one by making certain that the respective flagellar axes (each of which will be parallel to the relevant cell body axis) and cell body/flagellar joining points coincided. The amplitude and cone angle may then be defined from the 'envelope' of the tracings. The resulting set of tracings would represent the experimentally observed equivalent of Fig. 2. The cell body wave number $k=2\pi/\lambda$, amplitude α and axial extension are easily determined for the apparent centreline geometry of a constant-amplitude helix. Both the cell body length and the flagellar length are calculated (rather than measured) from equation 9, with $E(z)=0$ for the former case (see Ramia, 1991, for a more detailed discussion). The remaining parameters, the cell body radius a and the flagellar radius a_f , are essentially constant for this organism and are taken from a previous work (Swan, 1985), which shows scanning electron micrographs of *Spirilla*. On the provision that an allowance is made for the shrinkage due to fixation and critical-point drying of the cells, electron micrographs give a more reliable measure than cinemicrographs of the cellular dimensions. This is due to the higher resolution of electron micrographs. The resulting measured (and calculated) geometrical parameters are summarised in Table 1.

The absolute mean flagellar angular velocity $\bar{\omega}-\bar{\Omega}$ is simply determined by counting an exact number of flagellar cycles, multiplying by the film speed (in frames s^{-1}), dividing by the corresponding number of frames and finally multiplying by the factor 2π to convert the value into $rad\ s^{-1}$. A similar procedure follows for determining the absolute mean cell body angular velocity $\bar{\Omega}$, which consequently gives $\bar{\omega}$. Much like the numerical calculations, the mean swimming speed \bar{U} was defined by measuring the distance travelled along the axis of propagation, for an exact number of flagellar cycles, and dividing by the elapsed time. A summary of the measured and calculated mean swimming linear and angular speeds is given in Table 2 and these values are discussed below.

Observations of swimming trajectories were carried out by projecting the film onto a Watanabe DT1000 digitising tablet and digitising the coordinates of the cell body leading point *B* and the cell body/flagellar joining point *C* (as defined in Fig. 1) frame-by-frame. With every frame, the coordinates of the ocular graticule were also digitised and used as a

Table 2. *Summary of all measured and calculated mean swimming linear and angular speeds for each of the six cells*

Method	Quantity	Cell 1	Cell 2	Cell 3	Cell 4	Cell 5	Cell 6
Trailing flagellar configuration							
Experimental observations	$\bar{\omega}-\bar{\Omega}$ (rad s ⁻¹)	1074.425	779.115	238.761	339.292	502.655	188.496
	$\bar{\Omega}$ (rad s ⁻¹)	125.664	427.257	157.080	194.779	358.142	370.708
	$\bar{\omega}$ (rad s ⁻¹)	1200.088	1206.372	395.841	534.071	860.796	559.204
	\bar{U} (μ m s ⁻¹)	108	154	29	46	92	61
	$k\bar{U}/\bar{\omega}$	0.0407	0.0750	0.0465	0.0463	0.0672	0.0581
	$\bar{\Omega}/\bar{\omega}$	0.1047	0.3542	0.3968	0.3647	0.4161	0.6629
Theoretical calculations	$k\bar{U}/\bar{\omega}$	0.0457	0.0551	0.0468	0.0443	0.0547	0.0386
	$\bar{\Omega}/\bar{\omega}$	0.1905	0.2185	0.2187	0.2154	0.3126	0.5805
Leading flagellar configuration							
Experimental observations	$\bar{\omega}-\bar{\Omega}$ (rad s ⁻¹)	471.239	175.929	94.248	182.212	251.327	119.380
	$\bar{\Omega}$ (rad s ⁻¹)	395.841	345.575	87.965	270.177	521.504	314.159
	$\bar{\omega}$ (rad s ⁻¹)	867.080	521.504	182.212	452.389	772.832	433.540
	\bar{U} (μ m s ⁻¹)	95	47	3	27	95	51
	$k\bar{U}/\bar{\omega}$	0.0495	0.0529	0.0104	0.0321	0.0772	0.0626
	$\bar{\Omega}/\bar{\omega}$	0.4565	0.6627	0.4828	0.5972	0.6748	0.7246
Theoretical calculations	$k\bar{U}/\bar{\omega}$	0.0466	0.0554	0.0146	0.0271	0.0564	0.0439
	$\bar{\Omega}/\bar{\omega}$	0.2626	0.3065	0.0850	0.2095	0.4338	0.5126

reference point for the other coordinates. All frames digitised belonged to the same film sequence as that previously used to measure the swimming speeds and geometrical parameters. The resulting coordinates were stored in an ASCII (American Standard Code for Information Interchange) file, plotted on a spreadsheet program (Borland Quattro Pro for Windows), imported into a drawing package (Micrographics Designer 3.1 for Windows) and then scaled uniformly such that the body cylinder matched the dimensions of the cell body in question (here, cell 5) given in Table 1. Care was taken to confirm correct scaling by digitising the vertices of a $10\mu\text{m}\times 10\mu\text{m}$ square, and ensuring that it remained square at the end of all the plotting procedures.

Results

The results are presented in three separate subsections. A comparison between the experimental observations and BEM predictions of the mean swimming speeds for both leading and trailing flagellar configurations is presented first. The more detailed comparison of swimming kinematics is then considered. Finally, the performance of the present BEM model in comparison with previous models is assessed.

Comparisons of mean swimming speeds

Fig. 7A shows bar graphs of the normalised mean swimming speed $k\bar{U}/\omega$ for each of the six cells considered, swimming in the trailing flagellar configuration. It is noteworthy that both the BEM predictions and the experimental observations show the same general

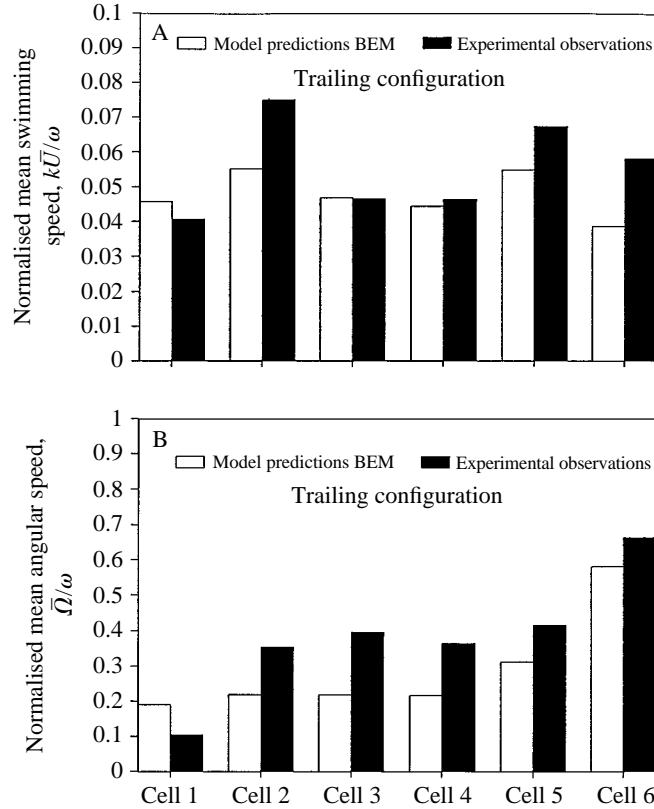


Fig. 7. Bar graphs showing the BEM-predicted and experimentally observed (A) normalised mean swimming speed, $k\bar{U}/\omega$, and (B) normalised mean angular speed, $\bar{\Omega}/\omega$, for each of the six cells swimming in the trailing flagellar configuration.

trend. The agreement between the BEM predictions and the experimental observations is generally good, with the BEM results usually underestimating the observed mean swimming speeds. However, the actual trend can only be explained in terms of the effects of changes in each of the geometrical parameters amongst the six cells. Based on the complete BEM model of Ramia (1991), these effects are briefly summarised in an approximate sense as follows. (1) As the normalised cell body wavenumber ak varies from 0.45 to 0.70, $k\bar{U}/\omega$ increases by approximately 30 % and $\bar{\Omega}/\omega$ decreases by approximately 20 %. (2) As the number of cell body wavelengths N_λ varies from 1.45 to 1.85, $k\bar{U}/\omega$ increases by approximately 10 % and $\bar{\Omega}/\omega$ increases by approximately 5 %. (3) As the normalised flagellar length l_f/l varies from 0.30 to 0.50, $k\bar{U}/\omega$ increases by approximately 50 % and $\bar{\Omega}/\omega$ increases by approximately 50 %. (4) As the flagellar cone angle (trailing case) γ varies from 50° to 85° , $k\bar{U}/\omega$ initially increases by approximately 10 % and then decreases by approximately 10 % again, and $\bar{\Omega}/\omega$ increases by approximately 40 %. (5) As the flagellar cone angle (leading case) γ varies from 60° to 85° , $k\bar{U}/\omega$ decreases by approximately 50 % and $\bar{\Omega}/\omega$ decreases by approximately 5 %. (6) As the normalised cell body radius a/l varies from 0.03 to 0.04, $k\bar{U}/\omega$ decreases by

approximately 10 % and $\bar{\Omega}/\omega$ decreases by approximately 10 %. (7) The normalised flagellar radius a_f/a is presumed to be constant at 0.2 for all six cells.

The BEM-predicted mean swimming speed $k\bar{U}/\omega$ for cell 2 shows a small increase over that of cell 1. To explain this, reference is made to the above-mentioned summary and Table 1. A very small increase results from minor increases in each of α_k and N_λ . Another small increase results from an increase in l_f/l , and no significant change results from a slight change in γ . Finally, a small increase in a/l leads to a small decrease in $k\bar{U}/\omega$ (as explained above). The net overall effect is an approximately 15 % increase in the BEM-predicted $k\bar{U}/\omega$ for cell 2, compared with that of cell 1. The trend for the BEM predictions of $k\bar{U}/\omega$ of the remaining four cells may be explained in a similar manner.

Fig. 7B shows bar graphs of the normalised mean angular speed $\bar{\Omega}/\omega$ for each of the six cells considered, swimming in the trailing flagellar configuration. Again both the BEM predictions and experimental observations show the same general trend. Furthermore, the BEM predictions generally underestimate the experimental observations to a greater extent than was the case for swimming speed (considered in Fig. 7A). The trend of these results may similarly be explained with the aid of the above summary and the changes in geometrical parameters as given in Table 1.

Fig. 8A shows bar graphs of the normalised mean swimming speed $k\bar{U}/\omega$ for each of the six cells considered, swimming in the leading flagellar configuration. Again both the BEM predictions and experimental observations show the same general trend. Of immediately apparent significance is the exceedingly low swimming speed for cell 3. This may be attributed mainly to the very large flagellar cone angle γ . As outlined in the above summary, Ramia (1991) predicts an approximately 50 % drop in $k\bar{U}/\omega$ as γ varies from 60° to 85° for a cell swimming in the leading flagellar configuration. To a lesser extent, the decreases in $k\bar{U}/\omega$ due to changes in both l_f/l and a/l also contribute to this. A similar explanation applies to the swimming speed of cell 4, which also has a large flagellar cone angle, namely 80° .

Fig. 8B shows bar graphs of the normalised mean angular speed $\bar{\Omega}/\omega$ for each of the six cells considered, swimming in the leading flagellar configuration. Again, both the BEM predictions and experimental observations show the same general trend. However, unlike the results of Figs 7A,B and 8A, there is a very large discrepancy between the BEM predictions and the experimental observations. This is likely to be a consequence of the more complex leading flagellar centreline geometry, which renders both the modelling and measurements of the relevant parameters γ and α_f (and consequently l_f) difficult. The propulsive torque is more heavily dependent on the flagellar centreline geometry than is the propulsive force (see Ramia, 1991; Myerscough and Swan, 1989). Because, for a linear fluid, the swimming speed is proportional to the propulsive force and the angular speed is proportional to the propulsive torque, it is natural to expect poorer agreement for the latter. This is also the case for the trailing flagellar configuration results of Fig. 7A,B, though to a much lesser extent.

Very little error is involved in the cell body wave parameters α_k and N_λ and consequently l , because they are measured with respect to the cell body centreline. An error, which may be up to 20 %, is involved in measuring the cell body and flagellar radii from scanning electron micrographs. The estimation of the flagellar parameters α_f and γ ,

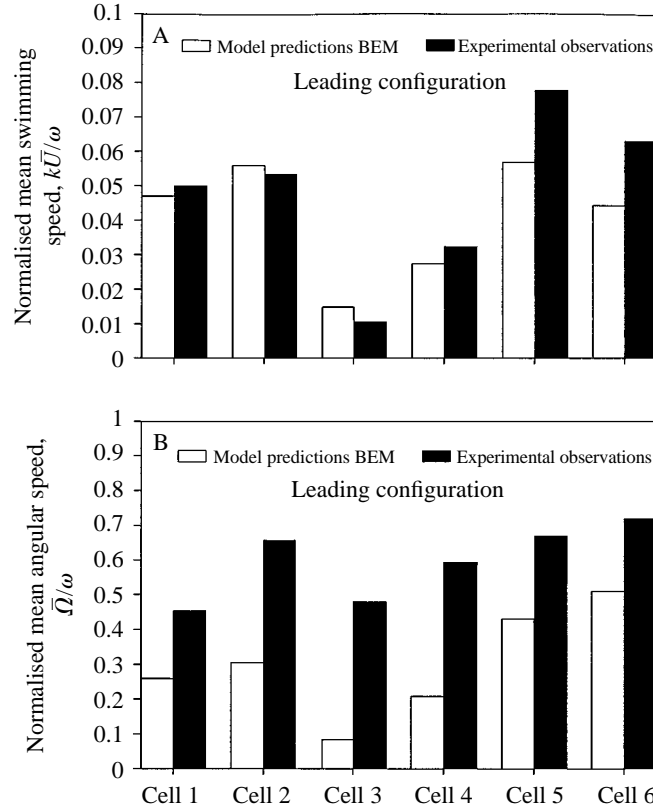


Fig. 8. Bar graphs showing the BEM-predicted and experimentally observed (A) normalised mean swimming speed, $k\bar{U}/\omega$, and (B) normalised mean angular speed, $\bar{\Omega}/\omega$, for each of the six cells swimming in the leading flagellar configuration.

however, was a little more vague. Certainly, the mathematically modelled geometries shown in Fig. 2 bear qualitative (and not quantitative) resemblance to the relevant observed flagellar geometries. This lack of an exact definition of the flagellar centreline geometry will inevitably lead to appreciable errors in the calculated flagellar length l_f and consequently in the predicted swimming linear and angular speeds. These may represent the major source of discrepancies between the measured and BEM-predicted results of Figs 7 and 8.

Comparisons of swimming trajectories

Keller and Rubinow (1976) considered the kinematics of an organism with a spherical cell body. They concluded that the trajectory of the cell body/flagellar joining point describes a helix about the axis of propagation, namely the Z -axis. Furthermore, the z -axis defines a constant angle with the Z -axis and precesses about it with a constant angular velocity depicting, in a frame at rest with respect to the joining point, a conical surface of revolution. This will hereafter be referred to as the cone of precession.

Ramia (1991) showed that, for any given geometrical parameters, the swimming

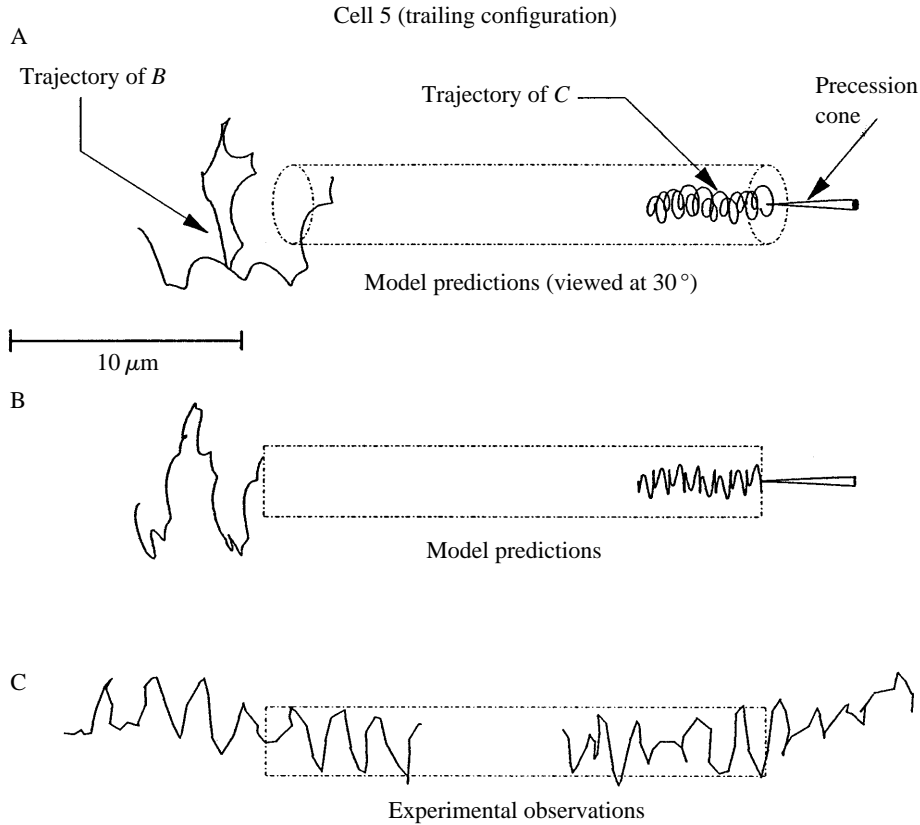


Fig. 9. Summary of the swimming kinematics for cell 5 swimming in the trailing flagellar configuration. (A) The BEM-predicted trajectories of the cell body leading point B and the cell body/flagellar joining point C , viewed at 30° to the X - Z plane, as well as the precession cone compared with the body cylinder. (B) Trajectories as in A, but viewed in the X - Z plane. (C) The experimentally observed trajectories, again viewed in the X - Z plane.

trajectories of *S. volutans* may be explained as minor generalisations of the trajectories predicted by Keller and Rubinow (1976). Namely, both the angle of precession (of the z -axis about the Z -axis) and the amplitude of the 'helical' trajectory of C vary periodically with each flagellar cycle. Geometrically, the cylinder defining the helical trajectory is replaced by the annular volume of two co-axial cylinders within which the point C is confined to move. Similarly (in a frame at rest with respect to the point C), the z -axis is confined to move within a conical shell of diminishing thickness at its apex.

Fig. 9A shows the BEM-predicted trajectories of the cell body leading point B and the cell body/flagellar joining point C , viewed at 30° to the X - Z plane, along with the precession cone, compared with the body cylinder for cell 5 in the trailing configuration. Fig. 9B shows the same trajectories viewed in the X - Z plane, whilst Fig. 9C shows the experimentally observed trajectories, again viewed in the X - Z plane. It is immediately apparent that, for the period of observation considered, there was an appreciable change

in the overall swimming direction. This cell rotated with a high cell body and flagellar frequency during the film sequence considered. Hence, with the film speed of $530 \text{ frames s}^{-1}$, only 6.5 frames per flagellar cycle were recorded. This, coupled with the fact that the points of interest *B* and *C* occasionally moved out of focus, made it impossible to resolve the intricate spirals of the BEM-predicted trajectories, if in reality they exist.

Initially, the point *C* was out of focus, and the organism was undergoing a change in swimming direction. The present BEM model precludes the possibility of a change in the swimming direction unless there exists a quiescent-flow inhomogeneity in the fluid, or a boundary or other foreign body. This is not a limitation of the BEM but a direct consequence of the modelled symmetrical rigid-body flagellar rotation. In fact, with the exception of the aforementioned conditions, this organism can only change the direction of its axis of propagation by executing an asymmetric flagellar rotation (or beat), which is not encompassed by the present BEM model. But, overlooking these initial effects, it is conceivable that the observed trajectories of *B* and *C* do represent a superposition of 'ideal corkscrew motion' (see Ramia, 1991) and precession (which was alternatively described by Myerscough and Swan, 1989, as pitching and yawing). Unlike the BEM predictions, the trajectories of *B* and *C* observed here appear to be of similar average amplitudes. This is an indication that the 'flexible' or 'inextensible' whip-like flagellar rotation has a distinctly different effect on the cell body kinematics than does the BEM-modelled rigid-body flagellar rotation. Albeit, the general qualitative agreement between the BEM-predicted and observed trajectories is good.

Fig. 10 shows the swimming kinematics results, both modelled and observed, as in Fig. 9, except that cell 5 was swimming in the leading flagellar configuration. There appears to be some change in the observed swimming direction in Fig. 10C, but to a much lesser extent than the trailing case of Fig. 9C. The cell body/flagellar joining point, in this case *B* (and not *C*), does exhibit an average amplitude, which is a little smaller than that of the trailing cell body point, in this case *C*. Although not as pronounced, this trend is consistent with the BEM predictions of Fig. 10B. Furthermore, the apparent agreement between the modelled and observed trajectories of *B* and *C* is better than that of the trailing case depicted in Fig. 9. This is due in part to the fact that both the cell body and the flagellum rotated much more slowly, giving nearly twice as many frames per flagellar cycle as were used during the trailing configuration.

A precession cone (which here degenerates into a triangle) was defined, from observations, by two lines whose directions define the respective extreme limits of the direction of the cell body axis. A smaller time interval (approximately three flagellar cycles) was considered for this, in which the organism was better behaved in maintaining a constant swimming direction. A substantially larger cone angle results than is predicted by the present BEM model, although the average amplitudes of the relevant trajectories would suggest the contrary. This apparent paradox may be due in part to the fact that the cell body centreline geometry was modelled as a helix of constant amplitude. Observations show that, in many cases, the cell body amplitude decreased towards either or both ends of the cell body. This was particularly evident for the longer cell bodies.

Given the present apparatus and strategy employed for the observation of swimming

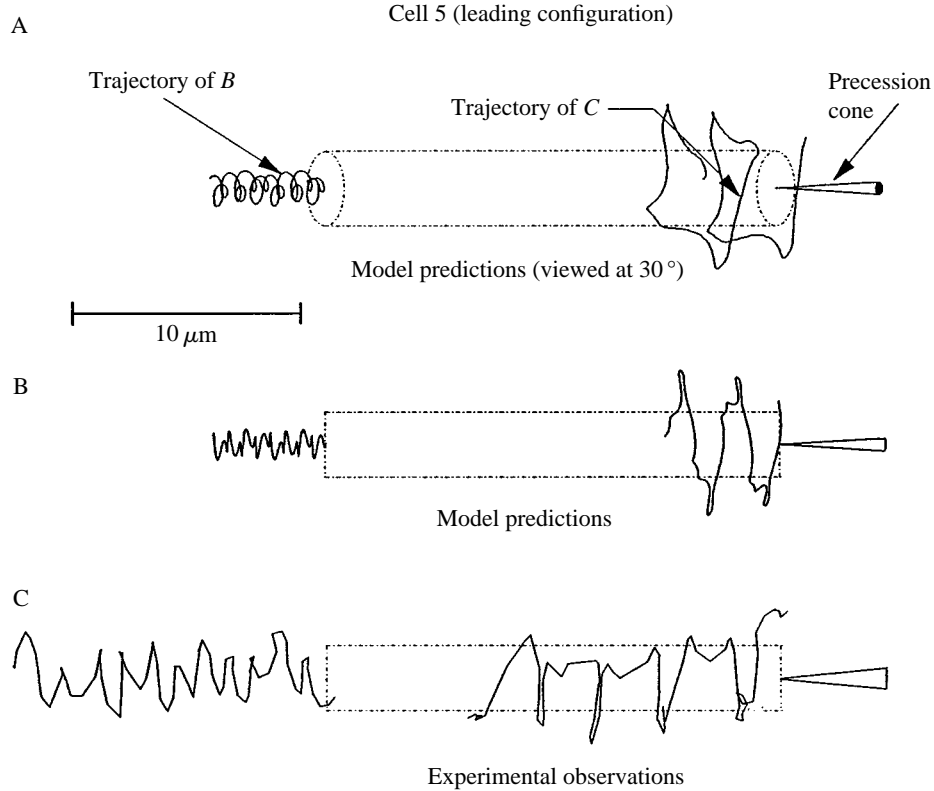


Fig. 10. Summary of the swimming kinematics for cell 5 swimming in the leading flagellar configuration. (A) The BEM-predicted trajectories of the cell body/flagellar joining point B and the cell body leading point C , viewed at 30° to the X - Z plane, as well as the precession cone compared with the body cylinder. (B) Trajectories as in A, but viewed in the X - Z plane. (C) The experimentally observed trajectories and precession cone, again viewed in the X - Z plane.

kinematics, a better comparison with the BEM predictions is not possible. A comprehensive experimental study of swimming kinematics should ideally involve measurements, with possibly a more representative number of instants per flagellar cycle, taken from two independent views (Teunis *et al.* 1992). This would yield a three-dimensional representation of the observed swimming kinematics which will inevitably compare more favourably with the three-dimensional BEM predictions.

Comparisons with previous models

A comparison, in a global average sense, of the present BEM predictions of the normalised mean swimming linear and angular speeds with those of experimental observations, RFT of Chwang *et al.* (1972) and SBT of Myerscough and Swan (1989) for the six cells is considered here. Table 3 summarises the relevant results. In each case, the average of the predicted swimming speeds amongst the six cells is considered. This

Table 3. Results due to the RFT model of Chwang *et al.* (1972), SBT model of Myerscough and Swan (1989), the present BEM model and experimental observations

Quantity	$k\bar{U}/\omega$	$\bar{\Omega}/\omega$
Unipolar <i>Spirilla</i> , trailing configuration		
RFT (Chwang <i>et al.</i> 1972)	0.0933	0.2910
SBT (Myerscough and Swan, 1989)	0.0279	0.1120
BEM (present study)	0.0475 ± 0.006	0.2894 ± 0.136
Experimental observations (present study)	0.0556 ± 0.012	0.3832 ± 0.162
Unipolar <i>Spirilla</i> , leading configuration		
RFT (Chwang <i>et al.</i> 1972)	0.0933	0.2910
SBT (Myerscough and Swan, 1989)	0.0279	0.1120
BEM (present study)	0.0407 ± 0.015	0.3017 ± 0.141
Experimental observations (present study)	0.0475 ± 0.021	0.5998 ± 0.100

Considered are the averages amongst the six cells, swimming in either the trailing or the leading flagellar configuration, of the normalised mean swimming speed $k\bar{U}/\omega$, and of the normalised mean angular speed $\bar{\Omega}/\omega$.

differs from the comparison considered by Ramia (1991), whose calculations were carried out for a single organism defined by a typical set of geometrical parameters.

The RFT model of Chwang *et al.* (1972) inherently neglects all hydrodynamic interaction and constrains the organism into moving only in the axial direction. For these reasons it merely gives an order-of-magnitude estimate of the normalised swimming speed in Table 3. The substantially better RFT estimate of $\bar{\Omega}/\omega$ in Table 3 is probably largely fortuitous. The fact that this model does not distinguish between leading and trailing configurations is clear evidence of this.

The SBT model of Myerscough and Swan (1989) performs a little better than that of Chwang *et al.* (1972), but consistently underestimates both the mean swimming linear and angular speeds. This SBT model does account for hydrodynamic interactions and allows the organism to move unconstrainedly in three dimensions. However, it remains limited to micro-organisms that can be modelled by a combination of slender bodies and spheroids, and it neglects the consideration of swimming kinematics. In fact, they define the mean swimming speed to be the arithmetic mean of the instantaneous swimming velocities throughout a given flagellar cycle. This definition of the mean swimming speed \bar{U} assumes the mean of the instantaneous velocities for a given flagellar cycle to be aligned with the axis of the cell body. It was shown that this axis (which is always parallel to the z -axis) consistently defines a finite angle of precession with the axis of propagation (Z -axis) throughout the swimming motion. For this reason, the arithmetic mean definition of \bar{U} overestimates the mean swimming speed. Hence, it would appear that applying kinematics to the results of the SBT model of Myerscough and Swan (1989) would serve to magnify further their discrepancy with experimental observations.

The BEM does account for hydrodynamic interaction, is generally applicable to organisms of any geometry and accounts for swimming kinematics. This is reflected by its good agreement with experimental observation of both the swimming linear and

angular speeds for the trailing flagellar case. For the leading flagellar case, however, good agreement exists only for swimming speeds and not for angular speeds. As explained above, this was mainly due to difficulty in modelling the leading flagellar centreline geometries.

Conclusions

High-speed bright-field phase-contrast cinemicrography has been used to record the movement of *S. volutans*. From these cine films, detailed measurements of geometrical parameters, swimming linear and angular speeds, as well as swimming trajectories, were made. Such detailed measurements were previously very difficult with traditional dark-field cinemicrography, owing to the scattering of light from the bright cell body (particularly when the cell was swimming in the leading flagellar configuration).

An existing BEM was used to model the swimming of this organism, and a cell-by-cell comparison, for all six cells in either the leading or trailing configuration, was drawn between the numerically predicted swimming linear and angular speeds and those experimentally observed. For a typical cell, a comparison of the swimming trajectories was also made. Good agreement for the mean swimming linear and angular speeds was apparent for all six cells in the trailing flagellar configuration. For the leading flagellar case, however, the mean swimming speeds compared favourably, whereas the mean angular speeds did not. This was mainly due to difficulty in modelling the leading flagellar centreline geometry, and the fact that $\bar{\Omega}$ depends more heavily on this geometry than \bar{U} . Given that two-dimensional observations of swimming kinematics were compared with the relevant view of three-dimensional BEM predictions, the swimming trajectories showed a qualitatively acceptable agreement. A fairer comparison would require measurements from two independent views giving a three-dimensional representation of the observed swimming kinematics (Teunis *et al.* 1992).

The SBT model of Myerscough and Swan (1989) is applicable only to slender bodies and spheroids and it neglects the consideration of swimming kinematics. The RFT model of Chwang *et al.* (1972) suffers these limitations, as well as neglecting all hydrodynamic interactions and constraining the organism to uni-axial motion. For these reasons, when compared with the present experimental observations, the present BEM model performed better than both of these previous models.

Appendix: discretisation and error

Each point on the surface of the cell body is considered to lie on the perimeter of a cross-sectional circle (centred about the centreline) of given constant radius (except very near the ends, where the radius decreases hemispherically to zero). The length of the cell body is discretised into 14 segments, by considering a finite number of cross sections, which are in turn discretised into polygons of seven sides. These polygons are then used to model the entire cell body surface by a series of septagonal cylinders sealed at either end by hemispherical domes. Every edge is then subdivided by an extra midside node, thereby defining an eight-noded curved parabolic element. Similarly, 14 segments and

five sides are used in discretising the flagellum, which is also closed off with a hemispherical dome at each of its two ends.

The method of determining the instantaneous velocities described above presupposes a finite cell body/flagellar separation distance. This is necessary to avoid numerical instability arising from nodes that are too close or coincident. Ramia *et al.* (1993) investigated the effects of this separation distance on the swimming speeds. They concluded that the swimming speeds are insensitive to variations in this separation distance, with the proviso that it should not exceed one flagellar radius a_f . Although they considered an organism of different geometry, we adopted a separation distance of $a_f/2$ throughout the present study, based on their findings.

An estimate of the discretisation error was gained by recalculating the swimming linear and angular speeds for a typical case using superparametric rather than isoparametric elements. For the former, a linear boundary solution along each element is presumed; for the latter, a quadratic solution is allowed. Comparison of the two types, for the given typical case, resulted in a difference of less than 0.5 %. A superparametric discretisation involves approximately 35 % of the number of colocation points that would be needed by a corresponding isoparametric discretisation. Given this, it may safely be concluded that the typical discretisation errors involved in the present BEM calculations are acceptably small.

Nomenclature and list of abbreviations

a	cell body radius
a_f	flagellar radius
\mathbf{A}^{-1}	a general three-dimensional rotation matrix
B	coordinates of the leading cell body point (Fig. 1)
BEM	boundary element method
C	coordinates of the trailing cell body/flagellar joining point (Fig. 1)
d_1, d_2	temporary parameters used in modelling flagellar geometry (Fig. 3)
dS	elemental surface area
$E(z)$	flagellar amplitude function (Fig. 3)
F, G	joining point and turning point used in modelling the leading flagellar geometry (Fig. 3)
$\mathbf{F}_1, \mathbf{F}_2$	forces experienced by the cell body and flagellum, respectively
\mathbf{G}, \mathbf{H}	known $3N \times 3N$ system matrices resulting from the boundary-integral formulation
H	point of inflection of the amplitude function $E(z)$
k	cell body wavenumber
k_e	parameter determining the rate at which the flagellum grows (with axial distance) to its maximum amplitude
k_f	flagellar wavenumber
l	cell body length
l_f	flagellar length
L	cell body axial extension (Fig. 1)
M	point defining the distal end of the flagellum (Fig. 3)

N_λ	number of cell body wavelengths
p	hydrostatic pressure
\mathbf{r}	position vector defining points on the cell body relative to the cell-body-fixed (x,y,z) frame (Fig. 5)
\mathbf{r}_f	position vector defining points on the flagellum relative to the cell-body-fixed (x,y,z) frame (Fig. 5)
\mathbf{R}	position vector defining points on the cell body relative to the globally fixed (X,Y,Z) frame (Fig. 5)
\mathbf{R}_C	position of the point C , the origin of the (x,y,z) axes, relative to the globally fixed (X,Y,Z) frame (Fig. 5)
\mathbf{R}_f	position vector defining points on the flagellum relative to the globally fixed (X,Y,Z) frame (Fig. 5)
RFT	resistive force theory
SBT	slender body theory
S_k	closed surface area of body k
t	time
\mathbf{t}	traction (local force per unit area)
$\mathbf{T}_1, \mathbf{T}_2$	torques experienced by the cell body and flagellum, respectively
\mathbf{u}	vector defining the velocity field on the surface of the organism
\mathbf{U}	instantaneous swimming velocity
$\mathbf{U}_1, \mathbf{U}_2$	instantaneous linear velocities of the cell body and flagellum, respectively
\bar{U}	mean swimming speed
\mathbf{V}	flow domain
\mathbf{x}	displacement vector from the cell body/flagellar joining point C
(x,y,z)	axes defining a frame at rest with respect to the cell body (i.e. the cell body frame)
(X,Y,Z)	axes defining the globally fixed frame of reference
z_e	axial extension of the flagellum
z_l, z_u	lower and upper limits, respectively, of integration for calculating the cell body and flagellar length
α	cell body amplitude (Fig. 1)
α_f	flagellar amplitude
γ	flagellar cone half-angle (Figs 1 and 3)
δ	flag variable distinguishing between points lying below and those lying above the turning point G of a leading flagellum
η	fluid viscosity
θ	flagellar phase angle ωt
λ	cell body helical wavelength (Fig. 1)
ψ_1, ψ_2, ψ_3	Euler angles as defined in Goldstein (1950)
ω	magnitude of the angular velocity of the flagellum relative to the cell body
$\boldsymbol{\omega}$	angular velocity of the flagellum relative to the cell body
$\boldsymbol{\Omega}$	instantaneous angular velocity of the cell body, i.e. of the organism
$\boldsymbol{\Omega}_1, \boldsymbol{\Omega}_2$	instantaneous angular velocities of the cell body and flagellum, respectively
$\bar{\Omega}$	mean swimming angular speed of the cell body

The experimental measurements were carried out through support to M.A.S. by the Australian Research Grants Scheme (ARGS). The present study was made possible by the work of Dr D. L. Tullock, who was originally responsible for the numerical implementation of the general Linear Three Dimensional Boundary Element Method (LTDBEM) program.

References

- BATHE, K. J. (1982). *Finite Element Procedures in Engineering Analysis*. Englewood Cliffs, New Jersey: Prentice-Hall.
- BERG, H. C. AND ANDERSON, R. A. (1973). Bacteria swim by rotating their flagellar filaments. *Nature* **245**, 380–382.
- BREBBIA, C. A., TELLES, J. C. F. AND WROBEL, L. C. (1984). *Boundary Element Techniques: Theory and Application in Engineering*. Berlin: Springer-Verlag. pp. 177–236.
- BRENNEN, C. AND WINET, H. (1977). Fluid mechanics of propulsion by cilia and flagella. *A. Rev. Fluid Mech.* **9**, 339–398.
- CHWANG, A. T., WINET, H. AND WU, T. Y. (1972). Locomotion of *Spirilla*. *Biophys. J.* **12**, 1549–1561.
- COX, R. G. (1970). The motion of long slender bodies in a viscous fluid. I. General theory. *J. Fluid Mech.* **44**, 791–810.
- GOLDSTEIN, H. (1950). *Classical Mechanics*. London: Addison-Wesley Publishing Co. Ltd.
- GRAY, J. AND HANCOCK, G. J. (1955). The propulsion of sea-urchin spermatozoa. *J. exp. Biol.* **32**, 802–814.
- HANCOCK, G. J. (1953). The self propulsion of microscopic organisms through liquids. *Proc. R. Soc. Lond. A* **217**, 96–121.
- HAPPEL, J. AND BRENNER, H. (1973). *Low Reynolds Number Hydrodynamics*. Leyden: Noordhoff International Publishing.
- HIGDON, J. J. L. (1979a). A hydrodynamic analysis of flagellar propulsion. *J. Fluid Mech.* **90**, 685–711.
- HIGDON, J. J. L. (1979b). The hydrodynamics of flagellar propulsion: helical waves. *J. Fluid Mech.* **94**, 331–351.
- JOHNSON, R. E. (1980). An improved slender body theory for Stokes flow. *J. Fluid Mech.* **99**, 411–431.
- KELLER, J. B. AND RUBINOW, S. I. (1976). Swimming of flagellated micro-organisms. *Biophys. J.* **16**, 151–170.
- LIGHTHILL, M. J. (1976). Flagellar hydrodynamics: The John von Neumann Lecture 1975. *SIAM Rev.* **18**, 161–229.
- MACNAB, R. M. AND ORNSTON, M. K. (1977). Normal-to-curly flagellar transitions and their role in bacterial tumbling. Stabilization of an alternative quaternary structure by mechanical force. *J. molec. Biol.* **112**, 1–30.
- MEISTER, M., CAPLAN, S. R. AND BERG, H. C. (1989). Dynamics of a tightly coupled mechanism for flagellar rotation. *Biophys. J.* **55**, 905–914.
- MUSSILL, M. AND JAROSCH, R. (1972). Bacterial flagella rotate and do not contract. *Protoplasma* **75**, 465–469.
- MYERSCOUGH, M. R. AND SWAN, M. A. (1989). A model for swimming unipolar *Spirilla*. *J. theor. Biol.* **139**, 201–218.
- PHAN-THIEN, N., TRAN-CONG, T. AND RAMIA, M. (1987). A boundary element analysis of flagellar propulsion. *J. Fluid Mech.* **184**, 533–549.
- RAMIA, M. (1991). Numerical model for the locomotion of *Spirilla*. *Biophys. J.* **60**, 1057–1078.
- RAMIA, M., TULLOCK, D. AND PHAN-THIEN, N. (1993). The role of hydrodynamic interaction in the locomotion of micro-organisms. *Biophys. J.* **65**, 755–778.
- SHIMADA, K., IKKAI, T., YOSHIDA, T. AND ASAKURA, S. J. (1976). Cinemicrographic analysis of the movement of flagellated bacteria. *J. Mechanochem. Cell Motil.* **3**, 185–193.
- SWAN, M. A. (1982). Trailing flagella rotate faster than leading flagella in unipolar cells of *Spirillum volutans*. *J. Bacteriol.* **150**, 377–380.
- SWAN, M. A. (1985). Electron microscopic observations of structures associated with the flagella of *Spirillum volutans*. *J. Bacteriol.* **161**, 1137–1145.

- TEUNIS, P. F. M., BRETSCHEIDER, F. AND MACHEMER, H. (1992). Real-time three-dimensional tracking of fast-moving microscopic objects. *J. Microsc.* **168**, 275–288.
- WINET, H. AND KELLER, S. R. (1976). *Spirillum* swimming: theory and observation of propulsion by the flagellar bundle. *J. exp. Biol.* **65**, 577–602.
- YOUNGREN, G. K. AND ACRIVOS, A. (1975). Stokes flow past a particle of arbitrary shape: A numerical method of solution. *J. Fluid Mech.* **69**, 377–403.